https://doi.org/10.5194/egusphere-2025-872
Preprint. Discussion started: 21 March 2025

The Component Summation Technique for Measuring Upwelling Longwave Irradiance in the Presence of an Obstruction

Bryan E. Fabbri[1,*], Gregory L. Schuster[2,*], Frederick M. Denn[1], Bing Lin[2], David A. Rutan[3], Wenying Su[2], Zachary A. Eitzen[3], James J. Madigan Jr.[1], Robert F. Arduini[4], and Norman G. Loeb[2]

[1]Analytical Mechanics Associates, Hampton, Virginia, USA
[2]NASA Langley Research Center, Hampton, Virginia, USA
[3]Adnet Systems Inc., Hampton, Virginia, USA
[4]Science Systems and Applications, Inc. (Ret.), Hampton, Virginia, USA
[*]Corresponding authors: Bryan E. Fabbri, bryan.e.fabbri@nasa.gov and Gregory L. Schuster, 91schuster@gmail.com

Abstract.

The CERES Ocean Validation Experiment (COVE) was an instrument suite located at the Chesapeake Light Station approximately 25 kilometers east of Virginia Beach, Virginia (36.9° N, 75.7° W). COVE provided surface verification for the Clouds and the Earth's Radiant Energy System (CERES) satellite measurements for 16 years. However, the large light station occupied approximately 15% of the field of view of the upwelling longwave flux measurement ($LW^{\uparrow}$), so radiation from the structure artificially perturbed the measurements. Hence, we use data from multiple instruments that are not influenced by the structure to accurately obtain $LW^{\uparrow}$; we call this the longwave component summation technique. The instruments required for the component summation are an infrared radiation thermometer to measure sea surface temperature, a pyrgeometer to measure downwelling longwave irradiance, and an air temperature probe. We find a strong negative bias between the obstructed upwelling pyrgeometer measurements and the component summation $LW^{\uparrow}$ in the colder months, less so in the warmer months. The bias ranged from -6% to +5% over COVE from 2004–2013. These range of biases are larger than the Baseline Surface Radiation Network (BSRN) targeted uncertainties of 2% or 3 W-m^{-2} (whichever is greatest), indicating that the component summation technique provides a significant correction to standard BSRN protocols when an obstruction is present. This work documents how we determine the component summation $LW^{\uparrow}$ irradiances and presents guidelines for how this method could be used at other locations.

1 Introduction

Atmospheric irradiance measurements in the shortwave (0.2-5 μm) and total (0.2-100 μm) channels are essential for characterizing the Earth's radiative energy budget (Wielicki et al., 1996). The Clouds and the Earth's Radiant Energy System

https://doi.org/10.5194/egusphere-2025-872
Preprint. Discussion started: 21 March 2025

(CERES) instruments have collected these vital measurements from multiple satellite platforms since 1997 with a third channel devoted to the window (8-12 μm) channel, which was replaced by the longwave band (5-35 μm) on the most recent platform (https://ceres.larc.nasa.gov/instruments/). These measurements play a vital role in assessing global temperature changes. CERES directly measures radiation at the top of the atmosphere, and the CERES team uses other measurements and methods to infer the radiation budget in the atmospheric column and at the surface. These level 3 products are not as robust as direct measurements, so the CERES project relies upon direct measurements from surface radiation sites located throughout the world for verification (Kratz et al., 2010).

One of these validation efforts was the CERES Ocean Validation Experiment (COVE), which was a suite of instrumentation that NASA maintained from 2000-2016 https://science.larc.nasa.gov/CRAVE/COVE. COVE was located at the Chesapeake Light Station (36.905N, 75.713W), a fixed platform located 25 km east of Virginia (near the mouth of the Chesapeake Bay). The Chesapeake Light Station was built in 1965 as a navigation aid to mark the entrance to the Chesapeake Bay and operated by the United States Coast Guard (USCG; https://www.lighthousefriends.com/light.asp?ID=1691, https://en.wikipedia.org/wiki-/Chesapeake_Light). The National Aeronautics and Space Administration (NASA) and the USCG formalized an inter-agency agreement in 1998 that allowed NASA to use the light station for solar radiation, aerosol, and meteorological measurements. The location and size of the Chesapeake lighthouse provided two characteristics that simplify atmospheric studies from the satellite viewpoint: 1.) a dark surface (the ocean), which simplifies retrievals of the optical properties of aerosols and clouds, and 2.) the lighthouse structure itself is small enough (25x25 meters) that the usual "island effect" associated with oceanic sites is negligible (MISR-Team, 2000; Rutledge et al., 2006).

Many surface radiation sites are networked with other sites that share databases and data acquisition protocols. This includes databases such as the Surface Radiation Budget Network (SURFRAD; https://gml.noaa.gov/grad/surfrad/), the Global Atmosphere Watch Station Information System (GAWSIS; https://gawsis.meteoswiss.ch/GAWSIS), and the World Radiation Monitoring Center (WRMC; https://bsrn.awi.de/project/objectives/) Baseline Surface Radiation Network (BSRN; https://bsrn.awi.de/). For example, COVE measurements adhere to standards set by the BSRN established in 1998 (Ohmura et al., 1998; Driemel et al., 2018). These standards include instrumentation with the highest available accuracy and high temporal resolution (1-3 minutes), near daily cleaning, and rigorous calibration protocols at regular intervals (usually yearly for shortwave and every few years for longwave and meteorological instruments). This renders the BSRN as the most highly-respected archive of long term surface radiation observations in the world, and is why the BSRN is the most commonly used data set for satellite validation of broadband shortwave and longwave radiation (Jin et al., 2003; Rutan et al., 2009, 2015; Kato et al., 2018).

Nearly all of the BSRN sites are located on land, which makes COVE unique as the only true water site in the BSRN database. COVE was located outside the surf zone and far enough away from shore to make it an excellent validation site for space-borne retrievals of cloud and aerosol microphysics. COVE provided better comparisons to satellite measurements than other scene types like snow, forest, desert, grassland, etc. (Belward and Loveland, 1996, and ceres.larc.nasa.gov/data/general-product-info/). Since the Earth is approximately 70% covered by water, validation of remote sensing algorithms over water is particularly important. COVE provided over 16 years of continuous surface radiation and aerosol measurements at the Chesapeake Light Station for validation of CERES and other satellite products (MISR, MODIS, SeaWiFS etc.). Observations

https://doi.org/10.5194/egusphere-2025-872
Preprint. Discussion started: 21 March 2025

ended in 2016 due to structural concerns. To our knowledge, no other ocean platform provided the type of continuity or quality equal to COVE (Rutledge et al., 2006).

Upwelling irradiance measurements over water are a challenge because 1.) They require a fixed platform in order to maintain a precise downward viewing geometry, 2.) The instruments must be mounted high enough above the water's surface to avoid spray, and 3.) The fixed platform should not occupy a significant portion of the instrument field of view (FOV); this is especially difficult for upwelling measurements over water.

There are other over-water sites that collect upwelling measurements, but many sites focus on measuring water-leaving radiances (e.g., to infer chlorophyll-a) and therefore are not impacted by the structure that supports the instruments (e.g., Hooker et al., 2003; Zibordi et al., 2006, 2009; Ha et al., 2019). As far as we know, the only other upwelling irradiance measurements collected at a site similar to COVE was an experiment at Buzzards Bay Entrance Light Station off the coast of Massachusetts, where Payne (1972) mounted shortwave pyranometers on a short 2 m boom to measure albedo. Not surprisingly, Payne (1972) also had obstruction issues and deleted the contaminated afternoon data.

At COVE, upwelling longwave radiation ($LW^{\uparrow}_{prg}$) was measured with an Eppley pyrgeometer (model PIR), which has a broadband spectral range of 4-50 µm. Ideally, pyrgeometers should be installed at a height of 30 m and located in a position with an unobstructed hemispherical FOV (McArthur, 2005). That installation was impractical at the Chesapeake Lighthouse. Thus, we located the upwelling instrumentation on an existing 8 m boom, 21 m above the surface. However, the 8 m boom length was insufficient to prevent the main structure from contributing a significant radiation signature to the pyrgeometer FOV. That is, the west side of the structure (where the boom is located) occupied an estimated 15% of the pyrgeometer scene from the service deck down to the mooring deck (see geometry in Figure 1 and Figure 2). This caused anomalies in pyrgeometer measurements that were inconsistent with the infrared radiation thermometer (IRT) measurements of the sea surface temperature (SST) at COVE.

Fortunately, there were other measurements at COVE that can be used to determine $LW^{\uparrow}$ without the upwelling hemispheric FOV pyrgeometer. Here, we describe how to use SST, downwelling longwave ($LW^{\downarrow}$), and temperature measurements in an energy balance equation to derive $LW^{\uparrow}$ values that are not affected by radiation emitted from the lighthouse. This component-summation technique allows us to recover 10+ years of $LW^{\uparrow}$ data at COVE that adheres to the rigorous BSRN target uncertainties and provides the best possible $LW^{\uparrow}$ measurements in the presence of an obstruction. We also discuss how our results can be applied to other locations with different measurement geometries and obstruction issues, and suggest that others use the $LW^{\uparrow}$ component summation technique to verify their own $LW^{\uparrow}$ measurements.

2 Motivation

The $LW^{\uparrow}$ measurement problem at COVE is illustrated quantitatively in Fig. 3, which presents differences between wide FOV upwelling pyrgeometer data and narrow FOV IRT data as a function of the solar geometry for the year 2008. The datapoints are very small so that daily data appear as U-shaped 'lines'. Winter months have the highest solar zenith angles at solar noon

https://doi.org/10.5194/egusphere-2025-872
Preprint. Discussion started: 21 March 2025

(when solar azimuth equals 180°), so lines for the winter season appear at the top of the figure. Likewise, the summer season occupies the lowest lines. The black dashed line in the middle represents the equinoxes.

One can follow a U-shaped line to surmise how the instrument differences vary throughout a day; the green and blue lines at the top of the figure indicate rather steady differences throughout winter days, whereas the lines below the equinoxes indicate $\sim$30 W-m^{-2} to $\sim$50 W-m^{-2} of variability throughout a typical summer day. The large range of biases (almost always positive) shown in Fig. 3 indicates that the lighthouse structure effect can be quite significant.

Ideally, the differences between the two measurements should remain steady throughout the day. However, the lighthouse structure has a different effective temperature than the water that it is blocking from the pyrgeometer, and this temperature difference has diurnal and seasonal cycles. It is also notable that the diurnal variability of the differences is greatest in the summer months, with the darkest reds occurring at azimuths between $\sim$ 200 and 300°. This is caused by the structure heating up throughout the clear-sky days while the ocean temperature remains steady.

Although the IRT measurements are useful for demonstrating the effect that the lighthouse structure has on the wide-FOV pyrgeometer measurements, the IRT measurements do not capture the reflected $LW^{\downarrow}$ or the air emission between the water and the pyrgeometer. We consider the effects of these additional components in Section 4 and demonstrate that the seasonal and inter-annual variability of this “lighthouse structure effect" is often greater than the maximum 2% bias recommended by the BSRN.

3 Instrumentation

The instruments used in this study are the following:

- **Pyrgeometers**: The pyrgeometer measures longwave irradiance. A pyrgeometer is intended for unidirectional operation in the measurement of $LW^{\downarrow}$ or $LW^{\uparrow}$ irradiance. We used a Precision Infrared Radiometer (PIR) from Eppley Laboratories. The angular FOV is 180° (hemispherical FOV is 2πsr). Spectral Range is approximately 4-50 µm and uncertainty is 5 W-m^{-2} (www.eppleylab.com/instrument-list/precision-infared-radiometer/). Calibrations were typically every 2-3 years.

- **Infrared Radiation Thermometer (IRT)**: The IRT measures the ocean skin temperature. It is a Heitronics model KT19.85 with a spectral range of 9.6-11.5 µm. This spectral range is where common atmospheric gases (including water vapor) do not absorb (i.e. atmospheric window). The lens used had an angular FOV of either 2.8°or 8.9°, depending on which instrument was in use during the calibration cycle. Accuracy is $\pm$ 0.5°C , plus 0.7% of the temperature difference between the housing containing the measuring instrument and the object to be measured (www.heitronics.com/wp-content/uploads/KT19.85-II-Datenblatt-EN-05.pdf). Calibrations were done typically every 1-2 years. The IRT was looking down at the water at an approximate 45°angle.

- **Meteorological**: Air temperature and Relative Humidity (RH) were measured with both a Vaisala (model CS500 and HMP50) and Rotronic (model HC-S3). Temperature accuracy is approximately $\pm$ 0.5°C for Vaisala and $\pm$ 0.3°C for Rotronic. The models listed above contain a Platinum Resistance Temperature detector to measure air temperature and require minimal maintenance. The RH from both the CS500 and HMP50 used an intercap sensor with accuracy of 3% between 10-90% RH and

https://doi.org/10.5194/egusphere-2025-872
Preprint. Discussion started: 21 March 2025

6% between 90-100% RH, with improved accuracy when switched to the Rotronic Hygroclip S3 sensor with accuracy of 1.5% (https://s.campbellsci.com/documents/us/manuals/cs500.pdf, https://s.campbellsci.com/documents/us/manuals/hmp50.pdf, and https://s.campbellsci.com/documents/ca/manuals/hc-s3_man.pdf). Temperature calibration and/or replacement of probes were conducted approximately every 2-3 years. In place of calibrations, the RH chip would be replaced as needed. Atmospheric pressure measurements were made with a Vaisala sensor, model PTB101B. The accuracy was ±0.5 mb at 20°C and ±1.5 mb from 0-40°C (https://s.campbellsci.com/documents/eu-/brochures/Manuals/ptb101b.pdf). Calibrations were made every 1-2 years.

- **Ground-Based Global Positioning System (GPS) Meteorology**: Measures integrated (total column) precipitable water vapor (in cm) in the atmosphere. Determined from a Global Positioning System (GPS) receiver and measured in centimeters every 30 minutes. GPS satellite observations are combined with GPS satellite orbit and Earth orientation parameters to estimate GPS signal delay (Zenith Total Delay or ZTD). Signal delays are then combined with surface meteorological information to estimate total precipitable water (Holub and Gutman, 2016). Meteorological calibrations generally occurred every 1-2 years, the physical GPS receiver did not require calibration.

4 Method

Although the lighthouse structure is a necessary fixture at COVE, it is also an undesirable interference that reduces the accuracy of the flux measurements. That is, the pyrgeometer measurements ($LW^{\uparrow}_{prg}$) at COVE had a portion of the FOV blocked by the Chesapeake Lighthouse (Figure 1 and Figure 2), so the measurements can be expressed as:

$$LW^{\uparrow}_{prg} = (1-f)LW^{\uparrow}_{f=0} + fLW^{\uparrow}_{twr}, \tag{1}$$

where f is the fraction of the pyrgeometer FOV that is blocked by the structure, $LW^{\uparrow}_{f=0}$ is the upwelling longwave in the absence of the structure, and $LW^{\uparrow}_{twr}$ is the longwave radiation emitted by the structure. Note that when f is small enough, $LW^{\uparrow}_{prg} \simeq LW^{\uparrow}_{f=0}$ and the pyrgeometer measurements accurately represent the upwelling longwave radiation. However, $f \simeq 0.15$ at COVE, so the pyrgeometer measurement does not accurately represent $LW^{\uparrow}_{f=0}$.

Nonetheless, we can also express $LW^{\uparrow}_{f=0}$ as a component summation of different measurements that do not require $LW^{\uparrow}_{prg}$ and are not influenced by $LW^{\uparrow}_{twr}$:

$$LW^{\uparrow}_{f=0} = (1-\varepsilon_1)[\varepsilon_w \sigma T_w^4 + (1-\varepsilon_1)(1-\varepsilon_w)LW^{\downarrow}] + \varepsilon_1 \sigma T_1^4, \tag{2}$$

where ε and T denote emissivities and temperatures of a medium, σ is the Stefan-Boltzmann constant (5.67×10^{-8} W-m^{-2} · K^{-4}), and $LW^{\downarrow}$ denotes the atmospheric downwelling longwave radiation measured at the site. The subscript 1 refers to the layer of air below the boom height, which we call Layer 1 (see ε_1 in Figure 1); the w subscript represents water. Water emissivity is $\varepsilon_w = 0.92$ (see Appendix B). This equation includes water emission after attenuation by the air below our sensors $[(1-\varepsilon_1)(\varepsilon_w \sigma T_w^4)]$, water reflectance after two-way attenuation by the air below our sensors $[(1-\varepsilon_1)^2(1-\varepsilon_w)LW^{\downarrow}]$, and emission of the air below our sensors ($\varepsilon_1 \sigma T_1^4$).

https://doi.org/10.5194/egusphere-2025-872
Preprint. Discussion started: 21 March 2025

Since Equation 2 is based upon multiple measurements that are not obstructed by the structure, we call Equation 2 the 'longwave component summation method' and restate it as:

$$LW_{cs}^{\uparrow} \equiv LW_{f=0}^{\uparrow} = (1-\varepsilon_1)[\varepsilon_w \sigma T_w^4 + (1-\varepsilon_1)(1-\varepsilon_w)LW^{\downarrow}] + \varepsilon_1 \sigma T_1^4. \tag{3}$$

However, we need to determine ε_1 before we can compute $LW_{cs}^{\uparrow}$.

4.1 Determining the Emissivity of the Air Below the Upwelling Instruments (Layer 1)

Calculating $LW_{cs}^{\uparrow}$ with Equation 3 is straightforward using measurements at COVE, except for the emissivity of Layer 1 (ε_1). However, the emissivity of the atmospheric column (ε_{atm}) ranges from $\sim$0.6-0.9 (Zhao et al., 2019, and discussion in Appendix A) and is relatable to ε_1. Additionally, we note that nearly all of the longwave absorption in the atmosphere is attributable to water vapor; hence, we determine the relationship between ε_1 and ε_{atm} by approximating the ratio of longwave optical depths (Layer 1 / atmospheric column) with the corresponding ratio of water vapor. That is, the scale factor η for the longwave optical depth can be expressed as:

$$\eta = \frac{\tau_1}{\tau_{atm}} = \left[\frac{Q_1 \rho_1 Z_1}{W}\right]. \tag{4}$$

Here, τ_1 and τ_{atm} denote the longwave optical depths corresponding to Layer 1 and the atmospheric column, and the term in the brackets is the ratio of the water vapor in Layer 1 to the column precipitable water vapor. The variables in the square brackets are determined by using four years of measurements (2004-2007) at COVE when precipitable water vapor was available: Q_1 is the water vapor mixing ratio obtained from temperature and pressure data (Wallace and Hobbs, 2006, page 82), ρ_1 is the density of dry air at standard temperature and pressure (1.225 kg/m^3), Z_1 is the boom height (21m), and W is the column precipitable water vapor obtained from GPS-Met (Holub and Gutman, 2016).

Recalling that transmissivity ($e^{-\tau}$) is related to emissivity by $e^{-\tau} = 1-\varepsilon$, Equation 4 can also be expressed as:

$$\eta = \frac{\ln(1-\varepsilon_1)}{\ln(1-\varepsilon_{atm})} = \left[\frac{Q_1 \rho_1 Z_1}{W}\right], \tag{5}$$

where ε_{atm} is the emissivity of the atmospheric column. Solving for ε_1, we obtain:

$$\varepsilon_1 = 1-(1-\varepsilon_{atm})^{\eta}. \tag{6}$$

Thus, we can compute the emissivity of the air below our sensors using the emissivity of the atmosphere and meteorological data obtained at the site. We do not have instrumentation for obtaining ε_{atm} (or τ_{atm}), but documented clear-sky atmospheric emissivities range from $\varepsilon_{atm} \simeq 0.6$ to 0.9 (e.g., Zhao et al., 2019), so we choose a midrange value of $\varepsilon_{atm} = 0.75$. We discuss the ramifications of this assumption in Appendix A. We used four years of meteorological data (2004-2007) with $\varepsilon_{atm} = 0.75$

https://doi.org/10.5194/egusphere-2025-872
Preprint. Discussion started: 21 March 2025

to obtain a median $\varepsilon_1 = 0.015$ and inter-quartile range = 0.007. We also note that the water vapor scale factor η at COVE has a median value of 0.011 over the same time period, with the 25-75 percentile ranging from 0.009 to 0.014. Liu (1986) found that η is relatively constant at ∼46 mid-ocean and small islands stations when $W \lesssim 4$ g-cm^{-2}, so it is not surprising that we found very little difference between using variable η obtained from meteorological data and using a climatological median for η; this is discussed further in Appendix A.

5 Results

Now that we have evaluated ε_1, we can quantify the component summation $LW^{\uparrow}_{cs}$ presented in Equation 3 and compare $LW^{\uparrow}_{cs}$ to the IRT measurements (in a similar fashion to the discussion in Section 2). We also determine $LW^{\uparrow}_{cs}$ for the 10 years of COVE data when we had IRT measurements.

5.1 Evaluating the Longwave Component Summation Method

Noting that $LW^{\uparrow}_{IRT} = \varepsilon_w \sigma T_w^4$, we solve Equation 3 for the difference between the component sum irradiance and the IRT measurements:

$$LW^{\uparrow}_{cs} - LW^{\uparrow}_{IRT} = -\varepsilon_1 \varepsilon_w \sigma T_w^4 + (1-\varepsilon_1)^2 (1-\varepsilon_w) LW^{\downarrow} + \varepsilon_1 \sigma T_1^4. \tag{7}$$

The significance of the various terms in Equation 7 are most easily explained by inserting $\varepsilon_1 = 0.015$ and $\varepsilon_w = 0.92$:

$$LW^{\uparrow}_{cs} - LW^{\uparrow}_{IRT} = 0.015 \times (\sigma T_1^4 - 0.92 \times \sigma T_w^4) + 0.078 \times LW^{\downarrow}. \tag{8}$$

Notice that the right hand side of Equation 8 is dominated by the reflected $LW^{\downarrow}$, since the coefficients for the atmosphere and water emission terms are a factor of 5 smaller than the coefficient for the longwave reflectance (i.e., $0.078/0.015 \simeq 5$). The air and water emission terms also tend to cancel one another, since $T_1 \simeq T_w$ on the Kelvin temperature scale. Taken together, they contribute less than 1 W-m^{-2} to Equation 8 when there is a 10 K temperature difference between the air and the water. Meanwhile, values for $LW^{\downarrow}$ at COVE are about 170 – 470 W-m^{-2}, so the 3rd term in Equation 8 contributes 13 – 37 W-m^{-2}. Thus, $LW^{\uparrow}_{cs} - LW^{\uparrow}_{IRT} \simeq (0.078) LW^{\downarrow}$ when $\varepsilon_w = 0.92$.

The diurnal variability of Equation 7 is shown in Figure 4. Note that the Summer afternoon 'hotspot' shown by the red points in Figure 3 does not occur in Figure 4 and that the pattern is much more symmetric after solar noon (i.e., symmetric after solar azimuth angle of 180 degrees). The biases still vary significantly between the Summer and Winter months, but this is because the reflected downwelling longwave ($0.078 \times LW^{\downarrow}$) is greater in the Summer than in the Winter.

5.2 Temporal Variations of Pyrgeometer Biases Caused by a Nearby Obstruction

The monthly and yearly relative biases of the pyrgeometer with respect to the component sum $LW^{\uparrow}_{cs}$ are summarized with boxplots in Figure 5. Boxes in the boxplots throughout this article indicate the interquartile range (IQR) and contain 50% of the data, the whiskers capture the 99 percentile, and the medians are denoted by red lines in the center of the boxes. All the

https://doi.org/10.5194/egusphere-2025-872
Preprint. Discussion started: 21 March 2025

boxplots have notches, which can barely be seen in Figure 5. The top and bottom edges of the notched regions correspond to median+$(1.57 \cdot IQR)/\sqrt{n}$ and median -$(1.57 \cdot IQR)/\sqrt{n}$. One can conclude with 95% confidence that the medians of two boxplots are different when the notches of the boxplots do not overlap (McGill et al., 1978). Lastly, the top X-axis has the percentage of data outside the BSRN target uncertainty of $\pm 2\%$ for each month, year and overall.

The left panel of Figure 5 presents the monthly variability of the $LW^{\uparrow}_{prg}$ bias relative to $LW^{\uparrow}_{cs}$ for 10 years of data (2004-2013). The absolute relative bias is largest in the coldest months and smallest in the warmest months. Although the median is within the 2% BSRN target uncertainty for every month, more than 25% of the data has biases greater than $\sim$2% for the winter months (Dec, Jan, and Feb) and one spring month (Mar). Additionally, the whiskers (lower and upper) indicate that 8 months have at least 15% of the data outside the target uncertainty; thus, a substantial portion of the pyrgeometer data do not conform to the BSRN target uncertainty. The amount of data outside the 2% target uncertainty ranges from 5.6% in August to 35.2% in January.

The right panels of Figure 5 show the inter-annual variability. Here again, the whiskers indicate that the pyrgeometer bias with respect to the component sum irradiance is greater than $\pm 2\%$ for a substantial portion of the data. The amount of data outside the target uncertainty range from a low of 10.8% in 2006 to a high of 26.9% in 2007. A three-year stretch from 2009-2011 have the lower quartile median near the edge of the target uncertainty, while 2013 has the upper quartile near the edge of the target uncertainty. This illustrates a large amount of data is outside the BSRN target uncertainty; we attribute this to the lighthouse structure influencing the $LW^{\uparrow}_{prg}$ measurements. The single box and whisker plot at the end of Figure 5 is the result of the entire 10 year period, regardless of month, and displays $\sim$17.7% of the data is outside the target uncertainty.

5.3 Single Day Scenarios

Figure 5 indicates that the lighthouse structure has the greatest effect on the pyrgeometer measurements in the winter months (e.g., January, December), which may seem counterintuitive. Hence, we analyze four single-day scenarios in winter and summer and in clear and overcast conditions to help understand the physics driving the statistics in Figure 5. Single-day continuous measurements are presented in Figures 6 and 7. Conventions used in both figures are as follows:

- Solid black lines represent the $LW^{\uparrow}_{prg}$ measurements and therefore include the lighthouse in the field of view.
- The light blue line is the water emission derived from the IRT ($LW^{\uparrow}_{IRT}$) and therefore does not include emissions from the lighthouse or the air above the water.
- The white line is derived from Equation 3 using $\varepsilon_1 = 0.015$.
- The red line is air temperature and red squares are water temperatures at selected times of the day (right Y-axis).
- Finally, the yellow shaded region denotes the solar elevation on that day (no scale).

The bias in $LW^{\uparrow}_{prg}$ caused by the lighthouse structure is clearly observed in the two winter scenarios of Figure 6. That is, $LW^{\uparrow}_{prg}$ (the black line) are noticeably lower than $LW^{\uparrow}_{cs}$ (white line) in Figure 6 throughout the day. This occurs when the

https://doi.org/10.5194/egusphere-2025-872
Preprint. Discussion started: 21 March 2025

air temperature is significantly colder than sea surface temperature; since the effective temperature of the lighthouse structure above water is likely close to the air temperature, the cold structure obscures some of the warm water in the pyrgeometer field of view and lowers the irradiance at the instrument location. It is also apparent that $LW^{\uparrow}_{prg}$ trends strongly with air temperature for the overcast winter day in the right panel of Figure 6 (comparing the red and black lines), further indicating that the structure temperature is tracking with the air temperature and affecting the pyrgeometer measurements. Meanwhile, $LW^{\uparrow}_{cs}$ is largely dominated by $LW^{\uparrow}_{IRT}$ and does not include any terms that are affected by the light station. Hence, the white line tracks $LW^{\uparrow}_{IRT}$ and are minimally affected by changes in the air temperature.

The differences between $LW^{\uparrow}_{cs}$ (white line) and the $LW^{\uparrow}_{prg}$ measurement (black line) is much greater on the clear winter day than the overcast winter day of Figure 6. This is because the temperature differential between the air and water is greater on the clear day than the overcast day. Nonetheless, we still see $LW^{\uparrow}_{prg}$ rapidly responding to air temperature changes in Figure 6 on the overcast day as a response to changes in the light station temperature. Note that the differences between $LW^{\uparrow}_{cs}$ and the $LW^{\uparrow}_{prg}$ measurement can be quite high on these winter days (up to $\sim$12 W-m^{-2} or 3.2%) which is outside the recommended BSRN target uncertainty of 2%. Finally, note that $LW^{\uparrow}_{prg}$ is always less than $LW^{\uparrow}_{cs}$ on both clear and overcast winter days because the structure is colder than the water when the air is colder than the water.

The lighthouse structure effect on the $LW^{\uparrow}_{prg}$ measurements is also distinct on the clear summer day shown in the left panel of Figure 7 (black line). Beginning with the pre-dawn portion of the day (i.e., solar azimuths less than $\sim 60°$), we see that $LW^{\uparrow}_{prg}$ is slightly greater than $LW^{\uparrow}_{cs}$. As the sun rises, the air temperature (red line), water temperature (red squares) and the $LW^{\uparrow}_{IRT}$ (light blue line) respond to the increasing insolation. The pyrgeometer (black line) responds dramatically to the heating of the lighthouse on this clear day when the structure is effectively warmer than the surrounding air in these conditions. Later in the day, the pyrgeometer responds to the decreasing insolation associated with lower solar elevation and returns to a value that is consistent with the previous night's value.

We see a different story on a summer overcast day shown in the right panel of Figure 7. Here, the nighttime air temperature before sunrise is about 1 K warmer than the water temperature, so the black line (pyrgeometer) is elevated above $LW^{\uparrow}_{cs}$ (white line). As the day progresses, the pyrgeometer responds to changes in air temperature and captures a blast of warm air after sunset. Here again, $LW^{\uparrow}_{cs}$ tracks the IRT measurements and does not directly respond to changes in air temperature. Thus, the component sum LW radiation ($LW^{\uparrow}_{cs}$, white line) tracks $LW^{\uparrow}_{IRT}$ (light blue line) on all four days in Figures 6 and 7 and is not sensitive to air temperature.

Finally, note that there is a period of time on the summer overcast day when the pyrgeometer provides the correct irradiance (from about solar noon until sunset in the right panel of Figure 7). This occurs when the water, air, and structure temperatures are in equilibrium (since the structure is at the same temperature as the water that it is blocking from the FOV of the pyrgeometer). It is also notable that the air and water temperatures also achieve equilibrium in the middle of the clear summer day (solar azimuth of 210°), but the pyrgeometer is biased about 14 W-m^{-2} high of $LW^{\uparrow}_{cs}$; this is because of the direct sun heating the lighthouse above the ambient air temperature.

In summary, the monthly LW flux biases in Figures 5 and the four daily scenarios of Figures 6 & 7 indicate that:

https://doi.org/10.5194/egusphere-2025-872
Preprint. Discussion started: 21 March 2025

1. Large and negative pyrgeometer biases (with respect to the component sum LW flux) occur in the winter because the lighthouse structure and air temperature are much colder than the water temperature this time of year.

2. Likewise, positive biases can occur on summer days when the lighthouse structure and air temperature are greater than the water temperature, especially on clear days when insolation directly warms the lighthouse structure.

3. The pyrgeometer provides the correct irradiance when the air temperature is in equilibrium with the water temperature in overcast conditions, which can occur any time of the year (per the range of values in the boxplots of Figure 5). However, this is not necessarily the case in clear-sky conditions.

6 Discussion

6.1 Alternate Geometries with Different Obstruction Issues

Thus far, we have presented results specific to the geometry of the COVE platform, which occupies 15% of the pyrgeometer FOV (i.e., $f = 0.15$). In this section we use the measurements at COVE to compute how measurements would be impacted if the platform geometry was different (i.e., $f \neq 0.15$).

First, we insert $f = 0.15$ into Equation 1 to describe the $LW^{\uparrow}$ measured with the pyrgeometer when an obstruction blocks 15% of the FOV:

$$LW^{\uparrow}_{p15} \equiv LW^{\uparrow}_{prg}(f = 0.15) = 0.85 \times LW^{\uparrow}_{f=0} + 0.15 \times LW^{\uparrow}_{twr}, \tag{9}$$

Solving both Equation 1 and Equation 9 for $LW^{\uparrow}_{twr}$ and equating the resulting expressions, we obtain an expression for the perturbation $LW^{\uparrow}_{prg'} - LW^{\uparrow}_{cs}$ associated with any value of f:

$$LW^{\uparrow}_{prg'} - LW^{\uparrow}_{cs} = \left[\frac{LW^{\uparrow}_{p15} - LW^{\uparrow}_{cs}}{0.15}\right] f, \tag{10}$$

where the prg' subscript indicates that the pyrgeometer is not fixed at a location where $f = 0.15$, and f can have any value between 0 and 1. COVE pyrgeometer measurements provide $LW^{\uparrow}_{p15}$, and $LW^{\uparrow}_{cs}$ is obtained from Equation 3 using the IRT, $LW^{\downarrow}$, and ambient air temperature (T_1) measurements at COVE. Dividing Equation 10 by $LW^{\uparrow}_{cs}$ yields the relative bias associated with the lighthouse structure perturbation:

$$\frac{LW^{\uparrow}_{prg'} - LW^{\uparrow}_{cs}}{LW^{\uparrow}_{cs}} = \left[\frac{LW^{\uparrow}_{p15} - LW^{\uparrow}_{cs}}{(0.15)LW^{\uparrow}_{cs}}\right] f. \tag{11}$$

which is shown for discrete values of f in Figure 8.

The box and whiskers at $f = 0.15$ in Figure 8 correspond to measurements at the COVE site, and is identical to the climatological box and whiskers for Years 2004-2013 in the rightmost panel of Figure 5. The remaining box and whiskers in Figure 8

https://doi.org/10.5194/egusphere-2025-872
Preprint. Discussion started: 21 March 2025

are obtained by computing the relative bias using variable f in Equation 11. As discussed earlier, more than 17% of the $LW^{\uparrow}_{prg}$ data at the COVE site has biases greater than the BSRN requirement of 2% (with respect to LW_{cs}). However, Figure 8 also indicates that the same dataset would produce biases of less than 2% for nearly all of the data if the pyrgeometer would have been located far enough away from the lighthouse such that $f \lesssim 5\%$. Unfortunately, the Chesapeake Lighthouse is so large that the pyrgeometer would need to be located on a 14m boom (an additional 6 m longer than the 8 m boom that is part of the Lighthouse) to achieve this level of agreement between $LW^{\uparrow}_{prg}$ and $LW^{\uparrow}_{cs}$. However, instruments located on platforms smaller than the Chesapeake Lighthouse should easily achieve $f \leq 5\%$, but this should always be verified before establishing new sites.

6.2 The Longwave Component Sum as a Residual Check for Longwave Flux Measurements

The BSRN protocols require some measurement redundancy in order to assure accuracy and mitigate data loss. For example, it is standard procedure for site managers to report shortwave irradiance using two different measurement techniques (Ohmura et al., 1998; McArthur, 2005; Driemel et al., 2018). These measurement techniques are 1.) The shortwave component-summation method, which sums direct normal irradiance measurements and shaded diffuse irradiance measurements, and 2.) the global method, which utilizes an unshaded pyranometer. The residual differences between these two methods are an important tool for verifying that the solar tracker is working properly.

In this section, we propose using Equation 3 as a component-summation method for $LW^{\uparrow}$. The basic premise is that all BSRN sites have $LW^{\downarrow}$ and ambient air temperature measurements, so the only additional instrumentation needed to compute $LW^{\uparrow}$ with Equation 3 is a precision IRT for obtaining T_w (or T_l over land). This redundancy could potentially discover a drifting pyrgeometer long before the instrument was due for calibration.

Additionally, this $LW^{\uparrow}$ component-summation approach could verify the quality of the pyrgeometer measurements at a site. For instance, Figure 5 demonstrates that the pyrgeometer measurements at the COVE site frequently do not meet the BSRN target accuracy (because the instrument is located too close to the structure). On the other hand, Figure 8 demonstrates that BSRN target accuracies could be achieved for 99% of the data for geometries where the structure obstruction occupies less than 5% of the field of view. Thus, the $LW^{\uparrow}$ component-summation technique can verify whether the structure obstruction is problematic for any BSRN site.

One potential drawback to the $LW^{\uparrow}$ component-summation technique is that the air and surface emissivities in Equation 3 are often unknown. The emissivity of the air below the instrumentation (ε_1) can be derived from Equations 4-6 using standard meteorological data and the column precipitable water vapor. However, ε_1 is small and the air below our pyrgeometer height of 21 m has very little effect on the irradiance. If column precipitable water vapor is not available, one can characterize the site with temporary measurements to determine a single characteristic ε_1 for that location. In our case, the impact of using a characteristic $\varepsilon_1 = 0.015$ instead of computing near instantaneous ε_1 had the highest maximum effect of $\sim\pm 0.4$ W-m^{-2} in the winter months and lowest maximum effect of $\sim\pm 0.2$ W-m^{-2} for spring (see Figure A1).

The other emissivity of concern in Equation 3 is ε_w, which needs to be replaced by its land-based cousin ε_l for land sites. Although water emissivity is characterized by $\varepsilon_w = 0.92$, land surface emissivity depends upon the surface type (sand, silt, clay, vegetation, snow, cement, etc.) and land surface moisture. Values range from about $\sim$0.85 to 0.97 for various land surface

https://doi.org/10.5194/egusphere-2025-872
Preprint. Discussion started: 21 March 2025

in the thermal infrared (Tian et al., 2019; Huang et al., 2016; Li et al., 2011), but surface emissivities could be lower in desert areas (https://www.jpl.nasa.gov). Site managers at non-water locations need to evaluate the surface emissivity at their sites and assess how the accuracy of their evaluation affects $LW^{\uparrow}_{cs}$ before adopting the LW component-summation method.

7 Conclusions

We have described a longwave component-summation method to measure upwelling longwave irradiance that does not include contributions from a host structure that supports the instruments. The technique requires a precision infrared thermometer, a $LW^{\downarrow}$ measurement (for water reflectance), meteorological data, and perhaps column precipitable water vapor measurements (to aid in characterizing the emissivity of the air below the measurements, depending upon location). We also present four case studies in different conditions (i.e., winter and summer, clear and overcast) and discuss the contributions of the radiative components term-by-term (i.e., water emission, longwave reflectance, and the air below the instruments) so that the reader can gain perspective about the relative importance of each of the terms.

Our longwave component-sum technique indicates that $LW^{\uparrow}_{prg}$ measurements display biases reaching 35% in January and 27% in 2007, with the strongest winter biases at COVE due to significant temperature differences between water and air during these months.

Overall, we find nearly 18% of the upwelling LW irradiance measurements are biased greater than the BSRN target uncertainty of 2% with respect to our component sum $LW^{\uparrow}_{cs}$. Thus, it is important to use the longwave component-sum technique whenever a host structure occupies a significant portion of the instrument field of view.

The Chesapeake Lighthouse uniquely occupies 15% of the field of view of the upwelling instruments. A determination was made using COVE data to compute the "lighthouse structure effect" that might be observed at different locations with different geometries. We found that geometries where the support structure occupies 5% or less of the instrument field of view will have biases of less than $\pm 2\%$ for 99% of the data.

We recommend the longwave component-sum technique as the primary upwelling longwave irradiance method for all sites that are located on ships or fixed structures over water.

We also provide some discussion about applying the longwave component-sum technique to land sites. The main challenge associated with applying the longwave component-sum method to land sites is to accurately assess the surface emissivity. Nonetheless, we propose that precision infrared thermometers be added to these surface radiation measurement sites as well, especially if land sites already collect $LW^{\downarrow}$ and air temperature measurements, since the longwave component-sum method can be used as a secondary method to monitor possible drift that may occur between calibrations of the primary irradiance measurements.

Data availability.

https://doi.pangaea.de/10.1594/PANGAEA.933174

https://doi.org/10.5194/egusphere-2025-872
Preprint. Discussion started: 21 March 2025

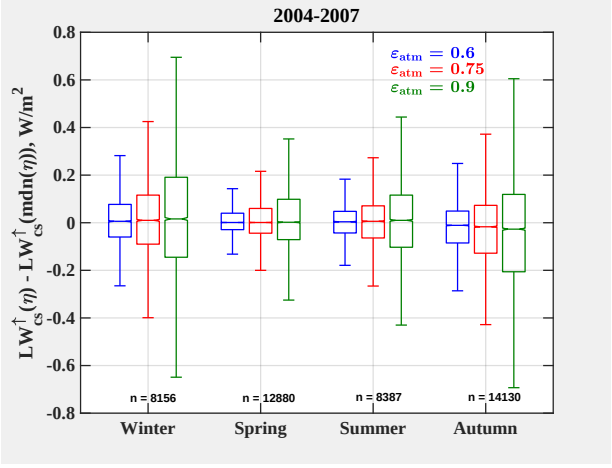

Figure A1. This plot assesses the range of $LW^{\uparrow}_{cs}$ values obtained using the median $\eta = 0.011$ in Equation 6 or using the available data at the COVE site; this is done for three ε_{atm} values (0.6, 0.75, 0.9). The range of values increase as ε_{atm} increases (i.e., the whiskers get bigger), but the median biases are near zero.

Appendix A: Sensitivity of ε_1 to Atmospheric Emissivity

In Section 4.1 we presented an average $\varepsilon_1 = 0.015$ for the layer of air below our sensors based upon Equation 6: $\varepsilon_1 = 1 - (1 - \varepsilon_{atm})^{\eta}$. We used a median scale factor of $\eta = 0.011$ in this equation derived from four years of water vapor mixing ratios and total column precipitable water vapor measurements at the COVE site (2004-2007). Equation 6 also requires the emissivity of the atmosphere, ε_{atm}; we used $\varepsilon_{atm} = 0.75$ based upon values found in the literature, as explained in the next paragraph. In this section, we explore the sensitivity of ε_1 to ε_{atm} and the effect of using $\eta = 0.011$ instead of using the range of η determined at the COVE site (IQR = 0.009 to 0.014).

Finding a robust emissivity of the atmosphere in the literature was a challenge. Some authors attempted to determine the atmospheric emissivity with clear skies (Staley and Jurica, 1972) or with clear skies at night (Chen et al., 1991), while others chose to determine the emissivity of air in a variety of conditions (Sridhar and Elliot, 2002; Abramowitz et al., 2012; Kalinowska, 2019). We concluded that ε_{atm} can not be precisely specified because of changing atmospheric conditions (e.g., cloud cover), but that reasonable values of ε_{atm} range from $\sim 0.6 - 0.9$ (Zhao et al., 2019). Thus, we chose $\varepsilon_{atm} = 0.75$ and show the impact of using $\varepsilon_{atm} = 0.6 - 0.9$ in Figure A1.

The median absolute differences in Figure A1 are near zero and the largest IQR is ~ 0.3 W-m^{-2} and occurs in winter when $\varepsilon_{atm} = 0.9$. Clearly, the range of η and ε_{atm} measured at COVE have little effect on $LW^{\uparrow}_{cs}$.

https://doi.org/10.5194/egusphere-2025-872
Preprint. Discussion started: 21 March 2025

Appendix B: Broadband Emissivity of Water

The broadband emissivity of water (ε_{wtr}) can be computed by weighting the spectral emissivity of water $\left(\tilde{\varepsilon}_{wtr}(\tilde{\nu})\right)$ with the Planck function:

$$\varepsilon_{wtr} = \frac{\int_{\tilde{\nu}_{min}}^{\tilde{\nu}_{max}} \tilde{\varepsilon}_{wtr}(\tilde{\nu}) B_{\tilde{\nu}} \tilde{\nu}}{\int_{\tilde{\nu}_{min}}^{\tilde{\nu}_{max}} B_{\tilde{\nu}} d\tilde{\nu}}, \tag{B1}$$

where $\tilde{\nu}$ is the wavenumber. The upwelling pyrgeometer measurement covers the 4-50 μm range, so $\tilde{\nu}_{min} = 200$ cm^{-1} and $\tilde{\nu}_{max} = 2500$ cm^{-1} for our measurements. The wavenumber form of the Planck function is expressed as

$$B_{\tilde{\nu}}(\tilde{\nu}) = 2hc^2\tilde{\nu}^3\left(\exp\left(\frac{hc\tilde{\nu}^3}{k_B T}\right) - 1\right). \tag{B2}$$

Here, $\tilde{\nu}$ has units of m^{-1}, $h = 6.626 \times 10^{-34}$ J-s is Plank's constant, $c = 2.998 \times 10^8$ m-s^{-1} is the speed of light, $k_B = 1.381 \times 10^{-23}$ J-K^{-1} is Boltzmann's constant, and T is the water temperature in Kelvin.

We use the spectral emissivity of calm water from Feldman et al. (2014) and the 1984-2008 median water temperature of 289 K at the lighthouse (https://www.ndbc.noaa.gov/data/climatic/CHLV2.txt) in Equations B2 and B1 to obtain $\varepsilon_{wtr,0} = 0.9147$. However, wind speed slightly increases the emissivity of water; the median climatological wind speed at the Chesapeake Lighthouse is 7.1 m-s^{-1}, which adds $\delta\varepsilon_{wtr,7} = 0.005$ to the calm water value (Huang et al., 2016). So the climatological-averaged broadband emissivity of water at the lighthouse is $\varepsilon_{wtr} = \varepsilon_{wtr,0} + \delta\varepsilon_{wtr,7} = 0.9147 + 0.005 = 0.92$.

We note that the wind speed and water temperature variations at the lighthouse do not significantly alter the seawater emissivity. The climatological record (1984-2008) indicates that the minimum and maximum seawater temperatures recorded at the lighthouse are 273 and 302 Kelvin. This corresponds to calm water emissivities in the range of 0.912-0.916, with the lowest emissivities occurring at the lowest temperatures. The interquartile range of wind speeds span 5-10 m-s^{-1}, and this adds 0.003-0.009 to the calm water emissivity (Huang et al., 2016). Since water temperature and wind speed are anti-correlated at the lighthouse (i.e., the coldest months are also the windiest months), the extreme range of emissivities is 0.919-0.921, or $\varepsilon_{wtr} = 0.92 \pm 0.001$.

Competing interests. The authors declare that there are no competing interests.

Acknowledgements. We thank the United States Coast Guard (USCG) and particularly Lt. Ed Westfall, Lt. Frank Minopoli, and Carlos Hernandez (BOSN, ATON officer Sector Hampton Roads) for allowing NASA CERES research at the Chesapeake Light Station. Likewise, we also thank the Department of Energy (DOE), Jim Green and Rick Driscoll for access to the Chesapeake Light after ownership transferred from the Coast Guard to the DOE in 2012. Finally, this work could not have been possible without funding from the NASA CERES project.

https://doi.org/10.5194/egusphere-2025-872
Preprint. Discussion started: 21 March 2025

References

Abramowitz, G., Pouyanné, L., and Ajami, H.: On the information content of surface meteorology for downward atmospheric long-wave radiation synthesis, Geophysical Research Letters, 39, 2012.

Belward, A. and Loveland, T.: The DIS 1km Land Cover Data Set, GLOBAL CHANGE, The IGBP Newsletter, 27, September, 1996.

Chen, B., Kasher, J., Maloney, J., Girgia, A., and Clark, D.: Determination of the clear sky emissivity for use in cool storage roof and roof pond applications, ASES Proceedings, Denver, CO, 1991.

Driemel, A., Augustine, J., Behrens, K., Colle, S., Cox, C., Cuevas-Agulló, E., Denn, F. M., Duprat, T., Fukuda, M., Grobe, H., Haeffelin, M., Hodges, G., Hyett, N., Ijima, O., Kallis, A., Knap, W., Kustov, V., Long, C. N., Longenecker, D., Lupi, A., Maturilli, M., Mimouni, M., Ntsangwane, L., Ogihara, H., Olano, X., Olefs, M., Omori, M., Passamani, L., Pereira, E. B., Schmithüsen, H., Schumacher, S., Sieger, R., Tamlyn, J., Vogt, R., Vuilleumier, L., Xia, X., Ohmura, A., , and König-Langlo, G.: Baseline Surface Radiation Network (BSRN): structure and data description (1992–2017), Earth System Science Data, 10, 1491–11 501, 2018.

Feldman, D., Collins, W., Pincus, R., Huang, X., and Chen, X.: Far-infrared surface emissivity and climate, Proc. Natl. Acad. Sci., 111, 16 297–16 302, https://doi.org/10.1073/pnas.1413640111, 2014.

Ha, K.-J., Nam, S., Jeong, J.-Y., Moon, I.-J., Lee, M., Yun, J., Jang, C. J., Kim, Y. S., Byun, D.-S., Heo, K.-Y., and Shim, J.-S.: OBSERVATIONS UTILIZING KOREA OCEAN RESEARCH STATIONS AND THEIR APPLICATIONS FOR PROCESS STUDIES, Bull. Am. Meteorol. Soc., 100, 2061–2075, 2019.

Holub, K. and Gutman, S.: Ground-Based Global Positioning System (GPS) Meteorology, Tech. Rep. Version 1.0, NOAA National Centers for Environmental Information (NCEI), 2016.

Hooker, S., Zibordi, G., Berthon, J.-F., D'Alimonte, D., van der Linde, D., and Brown, J.: Volume 23, Tower-Perturbation Measurements in Above-Water Radiometry, Tech. rep., NASA/TM-2003-206892, Vol. 23, 2003.

Huang, X., Chen, X., Zhou, D., and Liu, X.: An Observationally Based Global Band-by-Band Surface Emissivity Dataset for Climate and Weather Simulations, J. Atmos. Sci., 73, 3541–3555, https://doi.org/10.1175/JAS-D-15-0355.1, 2016.

Jin, Y., Schaaf, C. B., Woodcock, C. E., Gao, F., Li, X., Strahler, A. H., Lucht, W., and Liang, S.: Consistency of MODIS surface bi-directional reflectance distribution function and albedo retrievals: 2. Validation, J. Geophys. Res., 108(D5), doi:10.1029/ 2002JD002 804, 2003.

Kalinowska, M. B.: Effect of water–air heat transfer on the spread of thermal pollution in rivers, Acta Geophysica, 67, 597–619, 2019.

Kato, S., Rose, F., Rutan, D., Thorsen, T., Loeb, N., Doelling, D., Huang, X., Smith, W., Su, W., and Ham, S.: Surface Irradiances of Edition 4.0 Clouds and the Earth's Radiant Energy System (CERES) Energy Balanced and Filled (EBAF) Data Product, Journal of Climate Dynamics, doi: 10.1175/JCLI-D-17-0523.1, 2018.

Kratz, D., Gupta, S., Wilber, A., and Sothcott, V.: Validation of the CERES Edition 2B Surface-Only Flux Algorithms, J. Appl. Meteor. Climatol., 49, 164–180, https://doi.org/10.1175/2009JAMC2246.1, 2010.

Li, Z.-L., Wu, H., Wang, N., Qiu, S., Sobrino, J. A., Wan, Z., Tang, B.-H., and Yan, G.: Land surface emissivity retrieval from satellite data, International Journal of Remote Sensing, 34, 3084–3127, 2011.

Liu, T.: Statistical Relation between Monthly Mean Precipitable Water and Surface-Level Humidity over Global Ocean, Monthly Weather Review, 114, 1591–1602, 1986.

McArthur, L.: Baseline Surface Radiation Network (BSRN) Operations Manual, WCRP/WMO, WMO/TD-No. 1274 edn., 2005.

McGill, R., Tukey, J., and Larsen, W.: Variations of Box Plots, The American Statistician, 32, 12–16, 1978.

https://doi.org/10.5194/egusphere-2025-872
Preprint. Discussion started: 21 March 2025

MISR-Team: https://earthobservatory.nasa.gov/images/987/atmospheric-vortices-near-guadalupe-island, 2000.

Ohmura, A., Gilgen, H., Hegner, H., Müller, G., Wild, M., Dutton, E. G., Forgan, B., Fröhlich, C., Philipona, R., Heimo, A., König-Langlo, G., McArthur, B., Pinker, R., Whitlock, C. H., and Dehne, K.: Baseline Surface Radiation Network (BSRN/WCRP): New Precision Radiometry for Climate Research., Bull. Am. Meteorol. Soc., 79, 2115–2136, 1998.

Payne, R.: Albedo of the Sea Surface, Journal of the Atmospheric Sciences, 29, 959–970, 1972.

Rutan, D., Rose, F., Roman, M., Manalo-Smith, N., Schaaf, C., and Charlock, T.: Development and assessment of broadband surface albedo from Clouds and the Earth's Radiant Energy System clouds and radiation swath data product, J. Geophys. Res., 114, doi:10.1029/2008JD010 669, 2009.

Rutan, D., S.Kato, Doelling, D., Rose, F., Nguyen, L., Caldwell, T., and Loeb, N.: CERES Synoptic Product: Methodology and Validation of Surface Radiant Flux, Journal of Atmospheric and Oceanic Technology, 32, 1121–1143, 2015.

Rutledge, C., Schuster, G., Charlock, T., Denn, F., Smith, Jr, W., Fabbri, B., Madigan, J., and Knapp, R.: Offshore radiation observations for climate research at the CERES Ocean Validation Experiment, Bull. Am. Meteorol. Soc., 87, 1211–1222, https://science-data.larc.nasa.gov/CRAVE/papers/i1520-0477-87-9-1211.pdf, 2006.

Sridhar, V. and Elliot, R. L.: On the development of a simple downwelling longwave radiation scheme, Agricultural and Forest Meteorology, 112, 237–243, 2002.

Staley, D. and Jurica, G.: Effective atmospheric emissivity under clear skies, Journal of Applied Meteorology and Climatology, 11, 348–356, 1972.

Tian, J., Song, S., and He, H.: The relationship between soil emissivity and soil reflectance under the effects of soil water content, Physics of Chemistry and Earth, 110, 133–137, https://doi.org/10.1016/j.pce.2018.11.006, 2019.

Wallace, J. and Hobbs, P.: Atmospheric Science: An Introductory Survey, Elsevier, 2006.

Wielicki, B., Barkstrom, B., Harrison, E., III, R. L., Smith, G., and Cooper, J.: Clouds and the Earth's Radiant Energy System (CERES): An Earth observing system experiment, Bull. Am. Meteorol. Soc., 77, 853–868, 1996.

Zhao, D., Aili, A., Zhai, Y., Xu, S., Tan, G., Yin, X., and Yang, R.: Radiative sky cooling: Fundamental principles, materials, and applications, Applied Physics Reviews, 6, 021 306, 2019.

Zibordi, G., Holben, B., Hooker, S., Melin, F., Berthon, J.-F., Slutsker, I., Giles, D., Vandemark, D., Feng, H., Rutledge, K., Schuster, G., and Mandoos, A.: A Network for Standardized Ocean Color Validation Measurements, Eos Trans. AGU, 87, 293,297, 2006.

Zibordi, G., Holben, B., Slutsker, I., Giles, D., D'Alimonte, D., Melin, F., Berthon, J.-F., Vandemark, D., Feng, H., Schuster, G., Fabbri, B., Kaitala, S., and Seppala, J.: AERONET–OC: A network for the validation of ocean color primary products, J. Atmos. Oceanic Technol., 26, 1634–1651, 2009.

https://doi.org/10.5194/egusphere-2025-872
Preprint. Discussion started: 21 March 2025

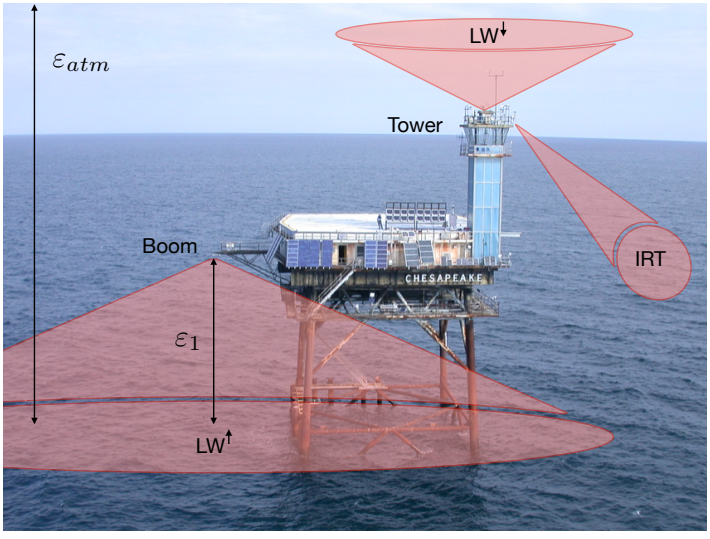

Figure 1. Illustration of the instrument geometry at the Chesapeake Lighthouse. $LW^{\uparrow}$ flux measurements are located on an 8 m boom, which is not long enough to remove the structure from the FOV. $LW^{\downarrow}$ flux measurements have an unobstructed FOV at the top of the lighthouse structure tower. The Infrared Radiation Thermometer (IRT) provides sea surface temperature, and it has a narrow FOV that is unobstructed by the structure. The emissivities ε_{atm} and ε_1 pertain to the atmospheric column and the layer of air below the boom.

https://doi.org/10.5194/egusphere-2025-872
Preprint. Discussion started: 21 March 2025

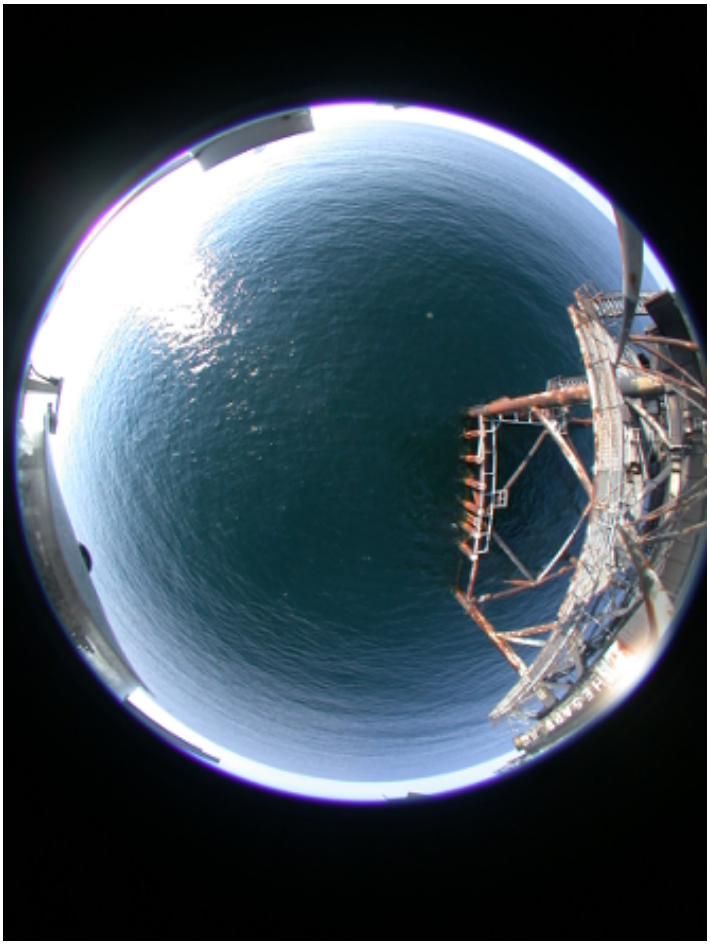

Figure 2. Fish-eye photograph taken near the end of the boom of Figure 1. The right side of the picture shows the lighthouse legs/structure occupying a significant portion of the static pyrgeometer FOV.

https://doi.org/10.5194/egusphere-2025-872
Preprint. Discussion started: 21 March 2025

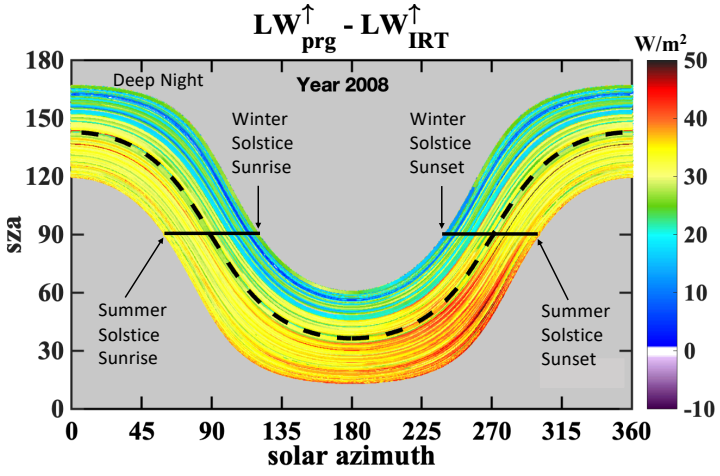

Figure 3. Single year plot of the differences between the upwelling irradiances measured with a pyrgeometer ($LW^{\uparrow}_{prg}$) and infrared radiation thermometer ($LW^{\uparrow}_{IRT}$). 445,578 points. The upper portion of the plot ($sza > 90$) is nighttime data and the lower portion ($sza < 90$) is daytime data; the dashed black line is the equinoxes, and azimuths greater than 180° occur after solar noon. Although a bias is expected (even in ideal cases) because the pyrgeometer captures longwave reflectance and atmospheric emission below the instrument that is not captured by the IRT, the dark red colors in the summer afternoons indicate that the pyrgeometer data is influenced by heat from the tower.

https://doi.org/10.5194/egusphere-2025-872
Preprint. Discussion started: 21 March 2025

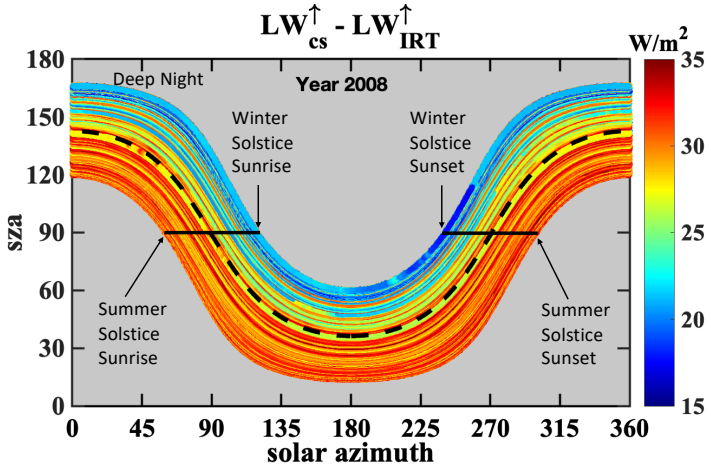

Figure 4. Similar dataset to Figure 3, but plot of the differences between the component sum longwave irradiance measurements defined in Equation 3 ($LW^{\uparrow}_{cs}$) and the IRT measurements. Notice the data is now symmetrical throughout the course of a day without the influence of the structure. There are still large biases between the summer and winter and this is due to the reflectance term being higher in the summer.

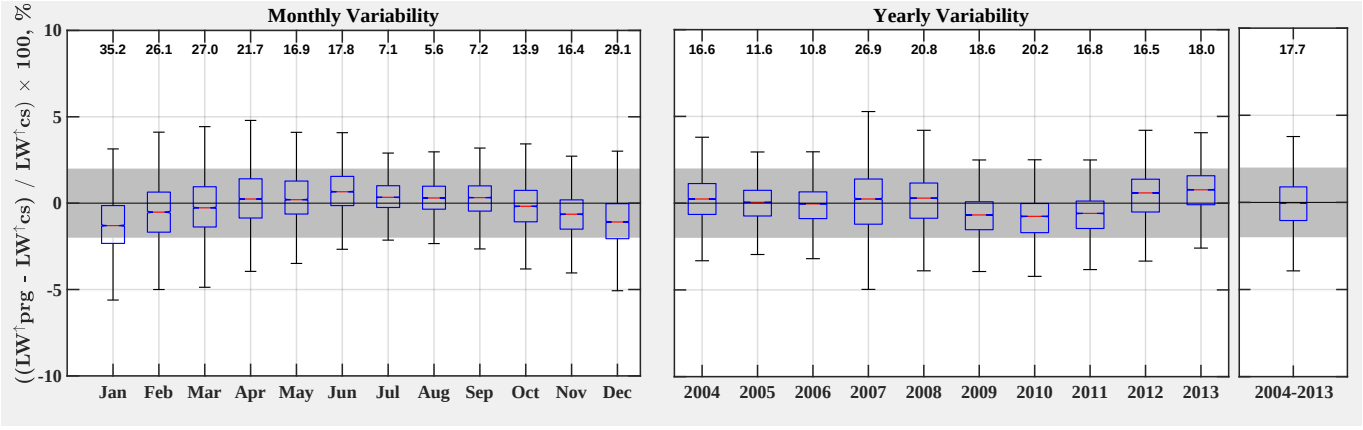

Figure 5. Monthly (left panel) and yearly (middle panel) boxplots of relative biases of the pyrgeometer measurements ($LW^{\uparrow}_{prg}$) with respect to the component summation measurements ($LW^{\uparrow}_{cs}$) over a 10 year period; the detached boxplot on the far right applies to all 10 years. The shaded region represents the BSRN targeted accuracy of $\pm 2\%$. The top X-axis indicates the percent data outside the target accuracy. Boxes capture the interquartile range (middle 50-percentile) and red lines represent medians. Notches (barely perceptible) indicate the uncertainty of the medians with an approximate 95% confidence level. Outliers are removed for visualization (defined as values that are more than 1.5 times the interquartile range) and whiskers represent the non-outlier minimums and maximums. Minimum number of points per box is 5505 for monthly boxplots and 8966 for yearly boxplots.

https://doi.org/10.5194/egusphere-2025-872
Preprint. Discussion started: 21 March 2025

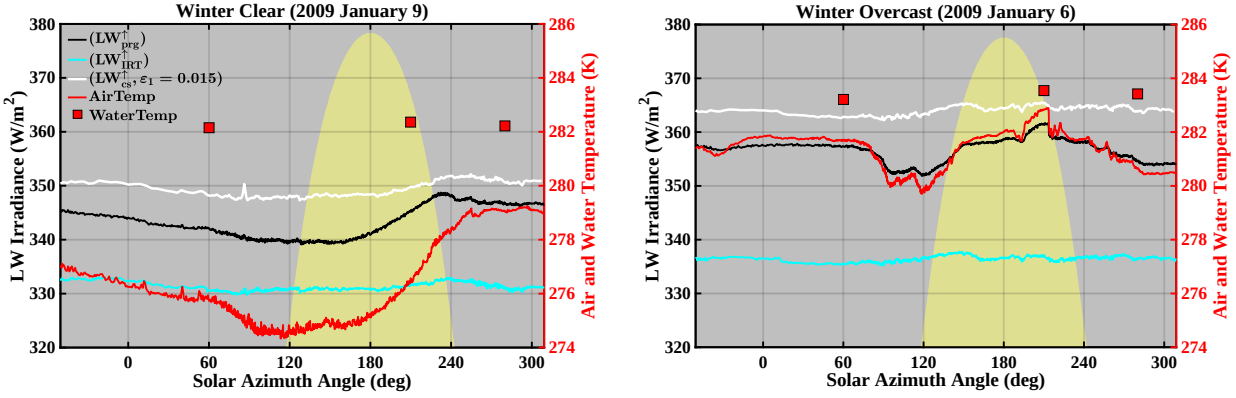

Figure 6. Longwave upwelling irradiances measured on two winter days; left panel is a clear day and right panel is an overcast day. Black lines: Pyrgeometer ($LW^{\uparrow}_{prg}$). Light blue: Infrared Thermometer ($LW^{\uparrow}_{IRT}$). White lines: Longwave component summation calculated using Equation 3 with $\varepsilon_1 = 0.015$ ($LW^{\uparrow}_{cs}$); this measurement is the most accurate of all irradiances in the figure. Red line: Air temperature (in Kelvin on the right Y-axis). Red squares: Water temperature (in Kelvin on the right Y-axis). Yellow shading: Solar elevation (not to scale). The pyrgeometer measurements (black line) are biased low of the longwave component summation measurements (white lines) because the cold lighthouse obstructs the field of view of the warm water.

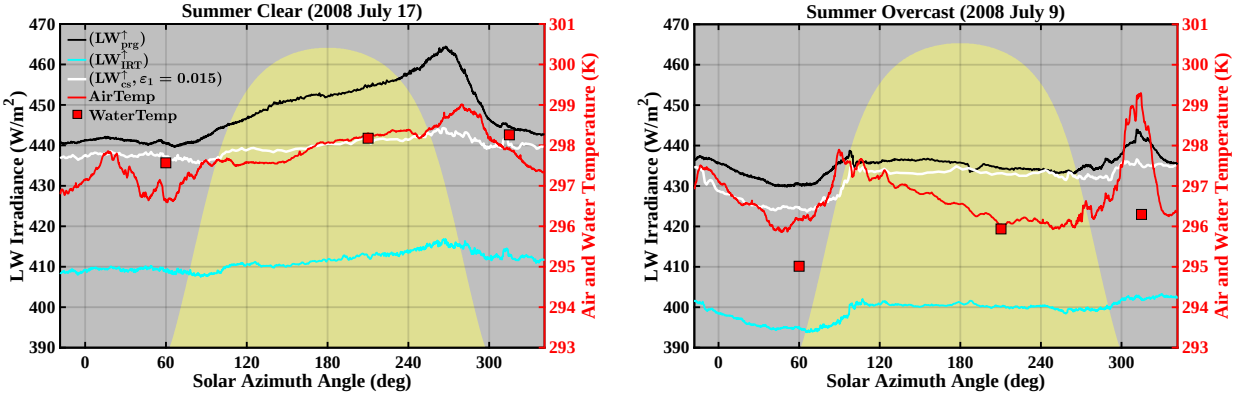

Figure 7. Longwave upwelling irradiances measured on two summer days; left panel is a clear day and right panel is an overcast day. The color schemes are the same as the winter days shown in Figure 6. The anomaly between the pyrgeometer measurements (black line) and the longwave component summation measurements (white lines) increases throughout the sunny summer day, indicating that the pyrgeometer is capturing the direct solar heating of the lighthouse structure. This direct solar heating does not occur on the overcast day, but the pyrgeometer does capture a blast of warm air that heats the lighthouse structure at sunset.

https://doi.org/10.5194/egusphere-2025-872
Preprint. Discussion started: 21 March 2025

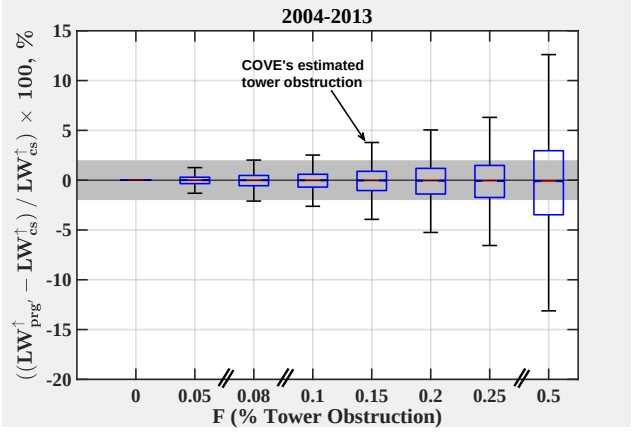

Figure 8. Computed relative biases associated with structures that obstruct different percentages of the field of view for hemispherical longwave measurements. Computations are based upon Equation 11 in Section 6.1. At COVE, the pyrgeometer had 15% structure obstruction. The pyrgeometer with 5% structure obstruction would be within BSRN target uncertainty. This would have required extending the boom at COVE an additional 6 m (14 m total) from where it was located.